**RESEARCH ARTICLE**

small methods
www.small-methods.com

# Geometrical- and Substrate-Dependent Photo Response of Thin-Film Silicon-Based Biointerfaces

*Lizhu Li, Yuxiao Zhang, Yunfei Gao, Yuqi Wang, Shirong Wang, Xue Gao, Ke Chen, Lan Yin, Xing Sheng,* and Dezhong Yao**

**Precise control of light-induced electrical signals at the biotic–abiotic interface remains a central challenge in advancing next-generation bioelectronic systems. In particular, achieving bidirectional signal modulation is essential for effective neural interface applications. Here, a spatially resolved, bidirectional photoelectric response at the silicon (Si) membrane–solution interface, induced by laser illumination is presented. Notably, a clear reversal in signal polarity between the illuminated regions (bright zones) and adjacent non-illuminated areas (dark zones) is observed. This signal orientation can be dynamically tuned by adjusting the light spot position and tailoring interfacial properties. To understand the underlying mechanism, the author systematically examined how various experimental parameters influence photoelectric behavior. These include the choice of adhesive, substrate conductivity (conductive vs insulating), boundary conditions (fixed vs free edges), and membrane geometry (e.g., grids and rectangles). These results reveal a cooperative effect between intrinsic charge conservation in the Si membrane and capacitive coupling at the interface. Moreover, in vivo studies show that integrating a conductive substrate beneath the Si membrane significantly enhances the modulation of sciatic nerve activity. Together, these findings define a new framework for light-responsive bioelectronic interfaces and point toward their broad utility in bioelectronic and neuromodulation applications.**

## 1. Introduction

Neuromodulation technologies have significantly advanced both our understanding of brain function and the clinical management of neurological disorders.[1–4] Recent developments include wearable neuromodulation systems capable of recording single-neuron and local field voltages in non-human primates and humans during both stationary and ambulatory states,[5,6] long-term deep brain stimulation and sensing devices designed to treat depression,[7,8] chronic wireless electrodes enabling adaptive stimulation for Parkinson's disease patients,[9] and spinal cord–muscle electrical interfaces that reconstruct sensorimotor pathways following spinal cord injury.[10] While electrical stimulation remains the clinical gold standard for neuromodulation, recent scientific advances have propelled optogenetics to the forefront of neuroscience research due to its cell-type specificity, spectral selectivity, and superior temporal and

---

L. Li, Y. Zhang, Y. Gao, D. Yao
The Clinical Hospital of Chengdu Brain Science Institute
MOE Key Lab for Neuroinformation
University of Electronic Science and Technology of China
Chengdu 611731, China
E-mail: dyao@uestc.edu.cn

Y. Zhang, Y. Wang, X. Sheng
Department of Electronic Engineering
Beijing National Research Center for Information Science and Technology
Institute for Precision Medicine
Center for Flexible Electronics Technology
IDG/McGovern Institute for Brain Research
Tsinghua University
Beijing 100084, China
E-mail: xingsheng@tsinghua.edu.cn

S. Wang, X. Gao
MegaRobo Technologies Co. ltd
Beijing 100085, China

K. Chen
Medical School
University of Electronic Science and Technology of China
Chengdu 611731, China

L. Yin
School of Materials Science and Engineering
The Key Laboratory of Advanced Materials of Ministry of Education
State Key Laboratory of New Ceramics and Fine Processing
Laboratory of Flexible Electronics Technology
Tsinghua University
Beijing 100084, China

L. Li, D. Yao
Sichuan Provincial Key Laboratory for Human Disease Gene Study and the Center for Medical Genetics
School of Life Science and Technology
University of Electronic Science and Technology of China
Chengdu 611731, China

The ORCID identification number(s) for the author(s) of this article can be found under https://doi.org/10.1002/smtd.202501228

**DOI: 10.1002/smtd.202501228**

spatial resolution.[11–13] However, its application in large mammalian brains continues to face major technical barriers and risks, including off-target effects and limited translational potential. These challenges have considerably hindered its clinical adoption.[14,15] In contrast, non-genetic optical stimulation techniques have gained growing interest.[16,17] These approaches integrate conventional silicon-based or organic optoelectronic components into neuromodulatory systems,[18] offering promising alternatives that avoid the genetic manipulation required by optogenetics while still enabling light-based neural control.

A growing number of optical strategies have emerged,[16,17] with the goal of replacing invasive, large-scale electrode arrays and enabling wireless neural stimulation. For example, ultrathin silicon (Si) membranes have been developed for cardiac pacing applications,[19–21] while various thin-film Si configurations have successfully modulated neuronal activity in models of dorsal root ganglion and cortical injury.[22] Similarly, semiconducting polymers such as poly(3-hexylthiophene) (P3HT) have demonstrated potential to restore light sensitivity in retinal explants from blind rodents.[16,23,24] These technologies offer key advantages, including wireless operation, low invasiveness, and high biocompatibility, which help overcome many limitations associated with traditional implanted electrodes, thereby presenting compelling alternatives for neuromodulation.[25–27] Looking ahead, such systems are poised to play a transformative role in biomedical and clinical applications.

Despite these advances, a deeper mechanistic understanding remains crucial for the precise deployment of silicon-based biointerfaces in complex biological environments. In particular, investigating both capacitive and Faradaic processes at the silicon–water interface[28] offers essential insights into the physicochemical interactions between silicon materials and biological fluids. These insights will inform the design of optimized silicon-based platforms for applications ranging from biosensing to targeted drug delivery. By examining the bidirectional voltage responses induced at silicon–water interfaces during mobile laser stimulation,[29,30] we can better characterize the underlying laser–interface interactions, surface charge redistribution, and associated electrochemical dynamics an important feature with potential to mimic neural signal encoding and enhance stimulation resolution.[31,32] Notably, prior studies have reported voltage inversion phenomena detected by photodetectors, which typically arise either from varying the wavelength of light sources[33–36] or from applying the same light source to different device configurations.[22]

In this study, we reveal a novel phenomenon that laser-localized illumination of Si membranes in solution generates reversed photoelectric signal distributions, creating counter-oriented and intensity-adjustable in-plane electric fields between illuminated and neighboring dark zones. We investigate the dynamic modulation of in-plane voltage gradients along the silicon membrane–solution interface by designing a series of experiments to characterize these spatial patterns. By precisely engineering boundary conditions, such as backside and lateral interfaces, and manipulating membrane geometries, including grid patterns and micropore arrays, we achieve fine spatiotemporal control over voltage polarity, magnitude, and spatial arrangement. Additionally, tuning the conductivity of adhesives and substrates further refines this control. This comprehensive strategy enables sophisticated modulation of photoelectric parameters, opening new avenues for applications requiring precise charge transport directionality and improved neural modulation capabilities. Our findings establish a physical framework for designing biological interfaces that regulate charge flow, advancing the development of next-generation wireless bioelectronics. Through systematic experimentation, we elucidate the fundamental mechanisms underlying voltage inversion and deepen understanding of charge transport across complex photo—liquid–solid multiphase interfaces. Furthermore, we define parametric relationships between interfacial properties and field modulation efficiency, providing critical design principles for future bioelectronic technologies.

## 2. Results

### 2.1. The Reverse Photovoltaic Phenomenon and its Mechanism

We fabricated pn-junction diodes using thin-film monocrystalline silicon by ion implantation of boron and phosphorus into n-type and p-type silicon wafers (n-Si and p-Si), forming $np^+$ and $pn^+$ Si membranes based on a silicon-on-insulator (SOI) structure. Gold nanoparticle treatment of these silicon films reduces surface impedance, enabling enhanced voltage signal detection. Upon immersing these membranes in phosphate-buffered saline (PBS) and irradiating them with a 635 nm red laser at controlled intensity, we observed the formation of opposing electric voltage fields between the illuminated and non-illuminated regions of the same Si membrane. This inverted voltage distribution was consistently detected not only in the fabricated $np^+$ and $pn^+$ membranes but also in undoped n-Si and p-Si membranes, indicating that the phenomenon arises from dynamic carrier redistribution within the Si rather than from specific doping profiles.

Traditionally, laser exposure generates electron–hole pairs in silicon, with their separation driven by the built-in electric field within the space charge region.[37] In $np^+$ membranes with the non-implanted surface facing upward, electrons migrate toward the n-region, while holes move toward the p-region. In freestanding membranes or those supported on non-conductive insulating substrates, this charge separation results in the local accumulation of one carrier type (e.g., holes) in the illuminated area. To maintain electrostatic balance, the opposing carrier (e.g., electrons) accumulates in adjacent dark zones, creating an in-plane voltage gradient across the surface (**Figure 1a**). This spatial redistribution of photogenerated carriers also drives the directional migration of ions within the PBS solution, further contributing to the observed photoelectric behavior.

Importantly, the voltage polarity difference between illuminated and dark zones strongly depends on the conductivity of the underlying substrate. When a conductive adhesive layer such as PEDOT: PSS establishes intimate contact between the Si membrane and a gold substrate, it forms a closed-loop, low-impedance pathway that rapidly extracts photo-generated charges. This efficient charge drainage prevents carrier accumulation in dark zones, thereby eliminating voltage inversion and producing a monotonic decay of voltage from the illuminated center outward (Figure 1b). Moreover, this conductive configuration amplifies the overall electric field strength by nearly threefold compared to freestanding membranes or those encapsulated with

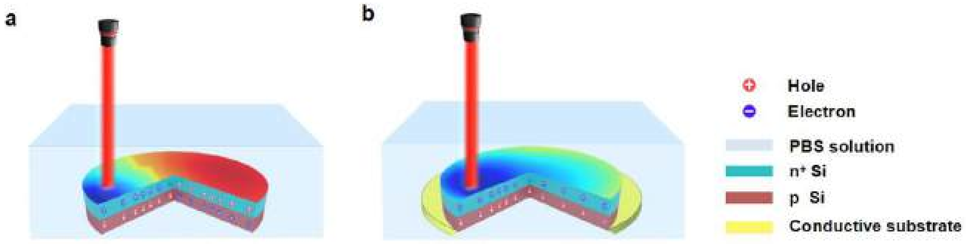

**Figure 1.** The reverse photovoltaic effect phenomenon and its mechanism. a) Cross-sectional schematic of pn$^+$ silicon with a non-conductive substrate in PBS buffer under light illumination. The dark region exhibits a voltage opposite to the illuminated area. b) Cross-sectional schematic of pn$^+$ silicon with a conductive substrate in PBS buffer under light illumination. The voltage gradually decreases with increasing distance from the illumination central.

insulating SU8 layers. This enhancement results from improved carrier transport and reduced recombination losses, emphasizing the pivotal role of interfacial charge extraction in optimizing optoelectronic device performance. These results establish a theoretical foundation for designing high-efficiency bioelectronic stimulation interfaces.

In summary, Si membranes paired with conductive metallic substrates achieve maximal electrical output when used as neural interfaces for biological tissue stimulation. This arrangement not only strengthens the electric field but also suppresses counterproductive voltage inversion caused by lateral carrier migration. Conversely, insulating substrates support dynamic spatial modulation of stimulation zones, providing versatile control for adaptive bioelectronic applications.

### 2.2. Mechanistic Analysis of Voltage Inversion via Interfacial Charge Dynamics

We fabricated four primary types of Si membranes: intrinsic p-type, intrinsic n-type, pn$^+$-type, and np$^+$-type, with respective thicknesses of 2.5, 25, and 16 μm. As shown in **Figure** 2a, a representative circular membrane with a thickness of 25 μm and a diameter of 5 mm was configured with the phosphorus-doped n$^+$-side oriented downward and the undoped p-side facing upward. We used a conductive PEDOT: PSS aqueous solution as the adhesive layer, and paired it with an interchangeable rigid gold substrate. Detailed fabrication procedures, material compositions, and instrumentation are described in the Experimental Section and Figure S1 (Supporting Information).

For optoelectronic measurements, we directed a vertically aligned 635 nm red laser beam with a fiber-coupled spot size of 200 μm onto the membrane surface. To map spatial voltage distributions across both illuminated and dark regions, we used a patch-clamp glass electrode integrated with an Ag/AgCl wire, precisely positioned using a micromanipulator[38] (Figure 2b). The energy band diagram of the illuminated pn$^+$-type membrane (Figure 2c) exhibits downward band bending at the interface between the p-type semiconductor and the electrolyte solution. Upon laser excitation, the membrane generates electron–hole pairs. Due to the stronger built-in electric field across the pn-junction relative to that at the semiconductor–solution interface, electrons are driven toward the n-region. This charge migration underscores the dominant role of the internal electric field in facilitating efficient carrier separation and transport within the Si membrane. Notably, charge transfer at the silicon-PBS interface equilibrates the system's Fermi level with the solution redox potential (Figure 2c). Photogenerated electrons, driven by conduction band energetics, accumulate at the surface and mediate reduction reactions—a Faradaic process evidenced by non-baseline-aligned voltage transients during illumination (**Figure** 3d). These light-triggered redox dynamics play an indispensable role in interfacial behavior under prolonged or intense illumination.

We elucidate the polarity inversion between illuminated and dark zones by thoroughly examining charge transport at the pn-junction and the Si-solution interface. When non-conductive substrates and adhesives are used, photo-generated carriers–holes in p-type regions and electrons in n-type regions-move laterally because vertical charge extraction pathways are absent. This confinement enforces charge conservation by causing opposite carriers to accumulate in the adjacent non-illuminated areas (Figure 2d). Specifically, in pn$^+$-type membranes, holes accumulate in illuminated p-regions, attracting anions from the surrounding PBS solution. Meanwhile, electrons accumulate in neighboring dark zones to maintain charge neutrality. Conversely, in illuminated n-regions, electron concentration dominates, balanced by hole accumulation in adjacent dark areas. This dynamic interplay reveals a complex equilibrium of carrier generation, lateral transport, and compensatory charge buildup between bright and dark zones.

To quantitatively describe this behavior, we model the system as a series of discrete longitudinal unit cells (Figure 2e), each represented by an equivalent circuit comprising: 1) resistive PBS electrolyte, which accounts for ionic collisions and associated resistance; 2) a capacitive double layer at the Si-solution interface, formed by electron–cation interactions on n$^+$ surfaces; 3) resistive p- and n-type bulk Si regions; and 4) a variable current source representing photo-generated carriers driven by illumination-dependent built-in electric fields. In insulating substrate configurations, the substrate interface acts as an open circuit, limiting charge dissipation. Upon initial illumination, transient capacitive charging produces voltage signals, which are recorded by the patch-clamp amplifier.

Using the pn$^+$ type Si film as an example, we focus on measurements at the p-side (Figure 2e). Considering the energy band barrier of the pn junction and the band bending that occurs at the Si-solution interface, vertical laser irradiation excites electron–hole pairs through photon absorption. Under illumination, holes accumulate on the p-side while electrons migrate toward the n$^+$ side. Simultaneously, surface charges are dynamically screened by double-layer interactions at the interface. In the adjacent dark

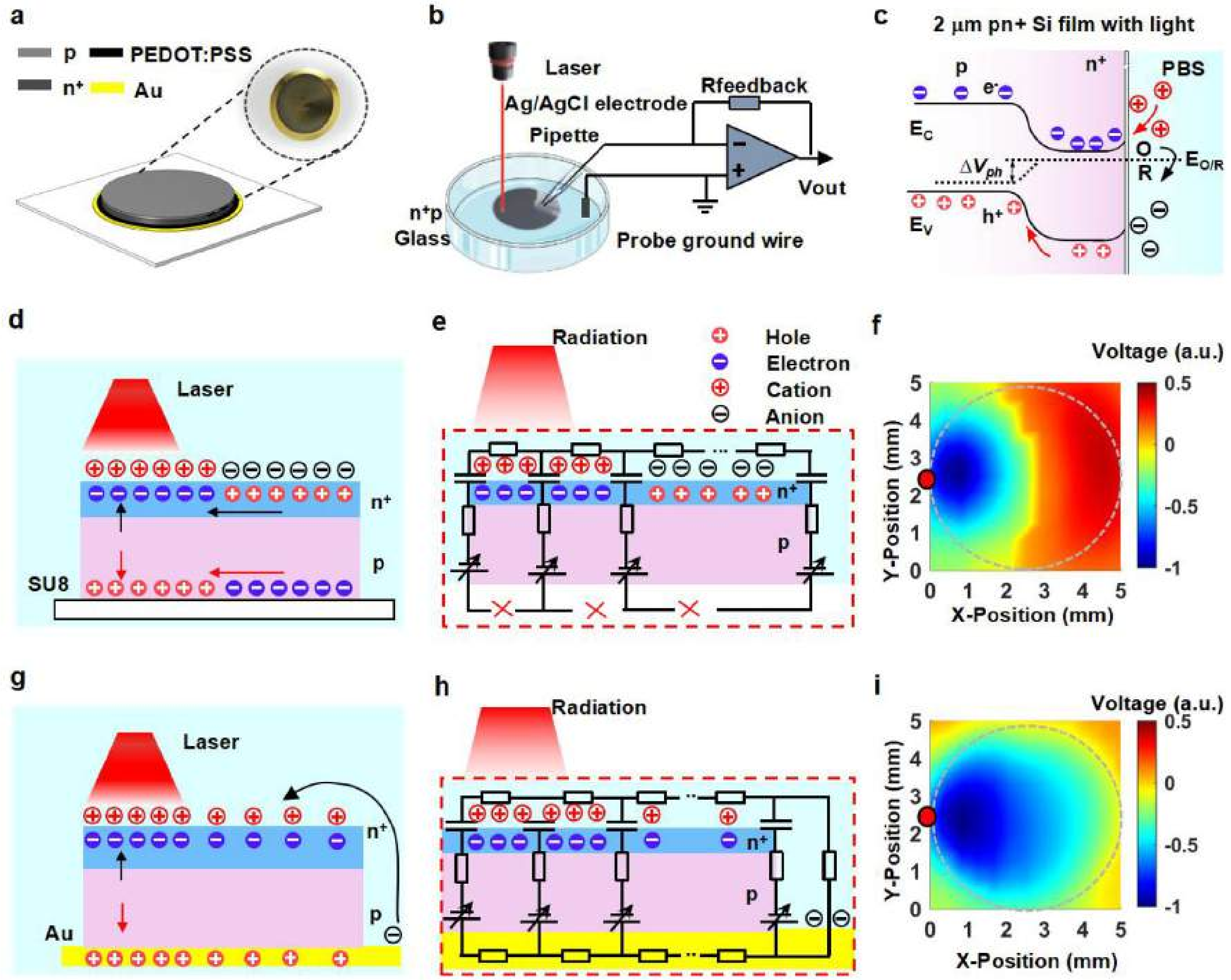

**Figure 2.** Mechanistic analysis of voltage inversion via interfacial charge dynamics. a) Schematic of freestanding silicon films (2.5 µm thick, 5 mm diameter) transferred onto glass substrates with gold, using PEDOT: PSS as an adhesive. b) Patch-clamp setup for measuring the photoresponse of the silicon thin film. A 635 nm laser (200 µm spot size) excites the photoelectric response in PBS solution, with photovoltaic voltage recorded in current-clamp mode. c) Band diagram illustrating photogenerated carrier flow (electrons, $e^-$ holes, $h^+$) in the pn junction and cation/anion accumulation at the Si/PBS interface under illumination ($pn^+$ Si film shown). Dashed lines indicate quasi-Fermi levels. d–f) Reverse surface voltage phenomenon in silicon films on insulating substrates. d) Carrier distribution at the pn junction and Si/PBS interface for a non-conductive substrate. e) Equivalent RC circuit model. f) Time-dependent voltage signals in illuminated and dark regions (non-conductive substrate, e.g., glass/SU8). The surface voltage heatmap reveals an inverted voltage distribution between light/dark zones. Grey dashed lines indicate the silicon film boundary; red circles mark laser illumination spots. g) Carrier distribution at the pn junction and Si/PBS interface for a conductive substrate. h) Equivalent RC circuit model. i) Time-dependent voltage signals in illuminated and dark regions (conductive substrate, e.g., Au/PEDOT: PSS). The surface voltage heatmap shows uniformly negative voltage across the film. Grey dashed lines indicate the silicon film boundary; red circles mark laser illumination spots.

region, charge conservation requires compensatory carrier accumulation to balance the deficit caused by photoexcitation. Minority carriers, specifically holes, accumulate in the $n^+$ side dark zone opposite the illuminated area. This redistribution leads to a reversal of the electrical voltage between the illuminated and non-illuminated zones on the same Si surface, producing the observed voltage polarity inversion.

This dual mechanism—vertical carrier separation driven by the pn junction coupled with lateral charge compensation—fully accounts for the voltage inversion observed in non-conductive systems. Our model aligns well with experimental results across multiple doping types and device geometries, establishing a universal framework for designing optoelectronic biointerfaces with precisely controllable electric field distributions. This framework provides a solid theoretical basis for future developments in the field. We employed a patch-clamp system paired with a maneuverable glass microelectrode to map the spatial distribution of photo-induced voltages. The microelectrode was raster-scanned over a square area encompassing the 5 mm-diameter Si membrane. Voltage maxima were recorded at predefined grid points, producing high-resolution voltage heatmaps (Figure 2f). For SU8-bonded membranes on glass substrates (non-conductive),

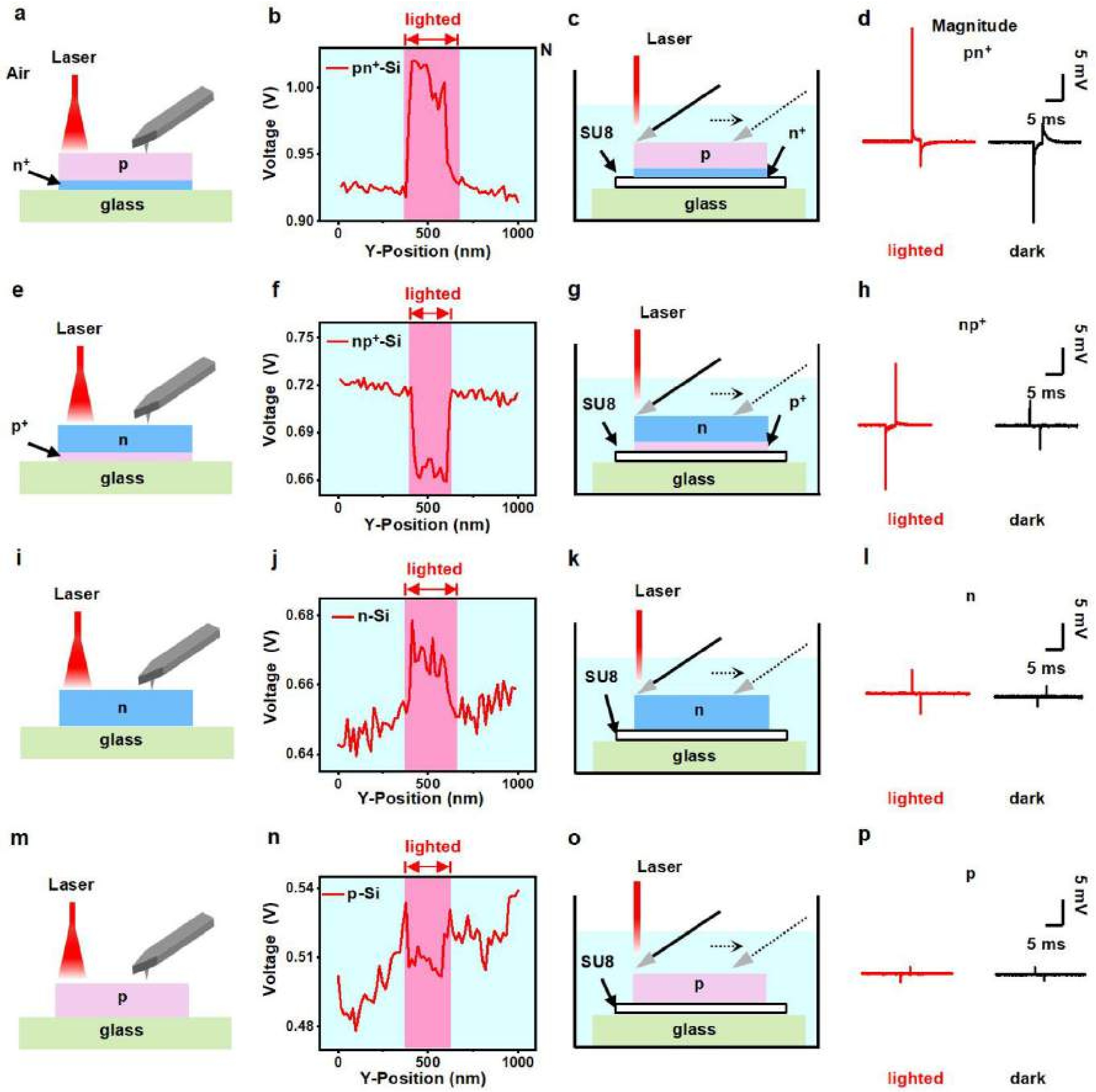

**Figure 3.** The critical role of interfacial environments. a) Schematic of AFM testing on a pn$^+$ sample in air. b) Surface voltage inversion in non-illuminated regions; illuminated areas show similar behavior to dark regions. c) Schematic of patch-clamp testing on a pn$^+$ sample in PBS solution. d) Voltage response to light activation: illuminated regions show an abrupt voltage increase while non-illuminated regions exhibit an instantaneous voltage drop. e) Schematic of AFM testing on an np$^+$ sample in air. f) Surface voltage decreases in non-illuminated regions; illuminated areas show similar behavior. g) Schematic of patch-clamp testing on an np$^+$ sample in PBS solution. h) Voltage response to illumination: decreases abruptly in light-exposed regions while increasing immediately in dark areas upon light activation. i) Schematic of AFM testing on an n-type sample in air. j) Surface voltage increases in dark regions; illuminated areas show identical behavior. k) Schematic of patch-clamp testing on an n-type sample in PBS solution. l) Voltage response to illumination: increases abruptly in light-exposed regions while decreasing immediately in dark areas. m) Schematic of AFM testing on a p-type sample in air. n) Surface voltage reduction in dark regions; illuminated areas show identical behavior. o) Schematic of patch-clamp testing on a p-type sample in PBS. p) Voltage response to illumination: increases in light-exposed regions while decreasing abruptly in dark areas.

polarity inversion begins near the geometric center (2.5 mm along the $x$-axis). The boundaries separating positive and negative voltages form arc-shaped contours that closely match the circular laser spot profile. These curved transition zones reflect the radial symmetry of lateral carrier redistribution constrained by the membrane edges.

By contrast, the PEDOT: PSS-Au configuration (conductive adhesive) effectively eliminated polarity inversion (Figure 2g). The conductive network enables seamless electron transfer from the $n^+$ region through the gold substrate, preventing charge accumulation in the dark zones. Consequently, free electrons accumulate on the exposed gold surface, attracting solution-phase cations that were previously localized in the p-side dark zones. This redistribution promotes hole diffusion-dominated behavior in the p-side dark zones, closely resembling the charge dynamics observed under illumination. Direct contact of the silicon film's n+ side with a conductor (such as Indium Tin Oxides (ITO)) similarly suppresses local charge accumulation, mirroring photovoltaic/photodetector architectures.[39] Top and bottom electrodes enable bidirectional carrier extraction and synergistically boost charge-carrier diffusion along the silicon film surface, amplifying lateral transport efficiency. The conductive system forms a closed-loop circuit (Figure 2h), where photo-generated charges at the variable current source (pn-junction) traverse bulk silicon resistances (p/n regions), interfacial capacitive double layers, and the PBS resistor, before returning via the gold substrate. This continuous pathway averts localized charge buildup and ensures voltage uniformity across the membrane. Spatial voltage mapping confirms the absence of polarity inversion in conductive setups (Figure 2i), showing a monotonic decrease in signal intensity with distance from the illumination center. This pattern sharply contrasts with that of insulating systems and highlights the essential role of substrate-mediated charge dissipation in preventing lateral compensation effects. In addition, the laser spots exhibit near-Gaussian profiles, with intensity peaking centrally and decaying radially. On conductive substrates, the voltage signal attenuates with beam-center distance (Figure 2i), directly tracking the local photoexcitation intensity. This spatial coupling confirms that optical excitation geometry governs signal amplitude, suggesting that expanded spot sizes or uniform LED illumination would enhance signal uniformity.

### 2.3. The Critical Role of Interfacial Environments

Previous studies have primarily focused on silicon morphologies such as porous and nanostructured forms;[21,40,41] however, investigating the silicon-biointerface remains equally important. As shown in Figure 3a,e,i,m, we used atomic force microscopy (AFM) to measure surface voltages of four silicon membrane types—$pn^+$, $np^+$, n-type, and p-type—under 635 nm laser irradiation (200 µm spot diameter) in air. Simultaneously, we recorded quantitative voltage signals in PBS using patch-clamp techniques. For the $pn^+$ and $np^+$ membranes, measurements targeted the non-implanted surfaces. During AFM scanning, the probe moves ≈0.4 µm over the sample, while an external 635 nm red laser irradiates either the scanned (illuminated) or non-scanned (dark) zones over a ≈0.2 µm length. A complete 1 by 1 µm voltage scan map is provided in Figure S2 (Supporting Information). AFM scans of the $pn^+$ silicon membrane in air yielded a full voltage map at 1 µm$^2$ resolution (Figure 3b). We redrew the perpendicular central line in this map for clarity. Comparing these results with solution-phase measurements (Figure 3c), we observe that illuminated areas show positive voltage, while adjacent dark regions exhibit negative polarity (Figure 3d). In contrast, $np^+$ membranes demonstrate decreased voltages in air at dark zones (Figure 3f) but show polarity inversion in solution (Figure 3g,h). Similar interface-dependent behaviors appear for n-type (Figure 3i–l) and p-type membranes (Figure 3m–p), measured both in air (Figure 3i,m) and in solution (Figure 3k,o). Notably, the 1.5 µm-thick p-type membranes display mechanical instability in air during AFM probing, likely due to deformation (Figure 3m).

Importantly, AFM grounding prevents voltage inversion in air by allowing efficient charge dissipation. By contrast, membranes immersed in solution without conductive pathways show polarity reversal in the dark zones. This difference arises from the dielectric properties at the interface: in solution, ionic compensation via double-layer capacitance enables dynamic charge equilibration. By comparison, air interfaces restrict charge redistribution to carrier recombination within the silicon bulk. Consistent with the finding, conductive substrates in PBS likewise suppressed voltage signal reversal (Figure 2g). Substrate conductivity enabled electron transfer to the gold surface, which has three advantages: i) prevented dark-region charge accumulation; ii) attracted P-surface cations from dark areas; and iii) established charge-balanced carrier diffusion (holes at p-surface, electrons at $n^+$-surface). This ionic redistribution enhanced bulk recombination in silicon. These results underscore the critical influence of interfacial ionic mobility on the relaxation behavior of photogenerated charges.

### 2.4. Boundary Condition Effects on Spatial Voltage Distribution

The heatmap derived from peak voltage signals visually captures the spatial distribution of voltage at the silicon–solution interface under illumination. To evaluate whether the surface charge distribution on the Si membrane is modulated by the adhesive solution or the underlying substrate, we tested two distinct adhesives: the insulating photoresist SU8-3005 and the conductive polymer PEDOT: PSS. In parallel, we paired these adhesives with four different substrates—glass, gold, ceramic, and ITO–coated conductive glass (**Figure 4a**)—to analyze variations in heatmap patterns upon laser exposure. As shown in Figure 4b, when SU8 is used as the adhesive with rigid substrates such as glass, gold, or opaque ceramic, the surface voltage on the Si membrane reverses polarity as the distance from the laser's focal point increases. In contrast, Figure 4c reveals that when PEDOT: PSS serves as the adhesive in combination with substrates like glass, gold, or ITO, the surface voltage of the Si membrane gradually diminishes, approaching zero with increasing distance from the irradiated center. These results demonstrate that while the substrate type exerts minimal effect on the heatmap when the adhesive remains constant, the voltage distribution varies significantly with changes in the adhesive solution—even when the substrate is unchanged. This highlights the adhesive layer as a primary factor in determining the surface voltage landscape under optical stimulation.

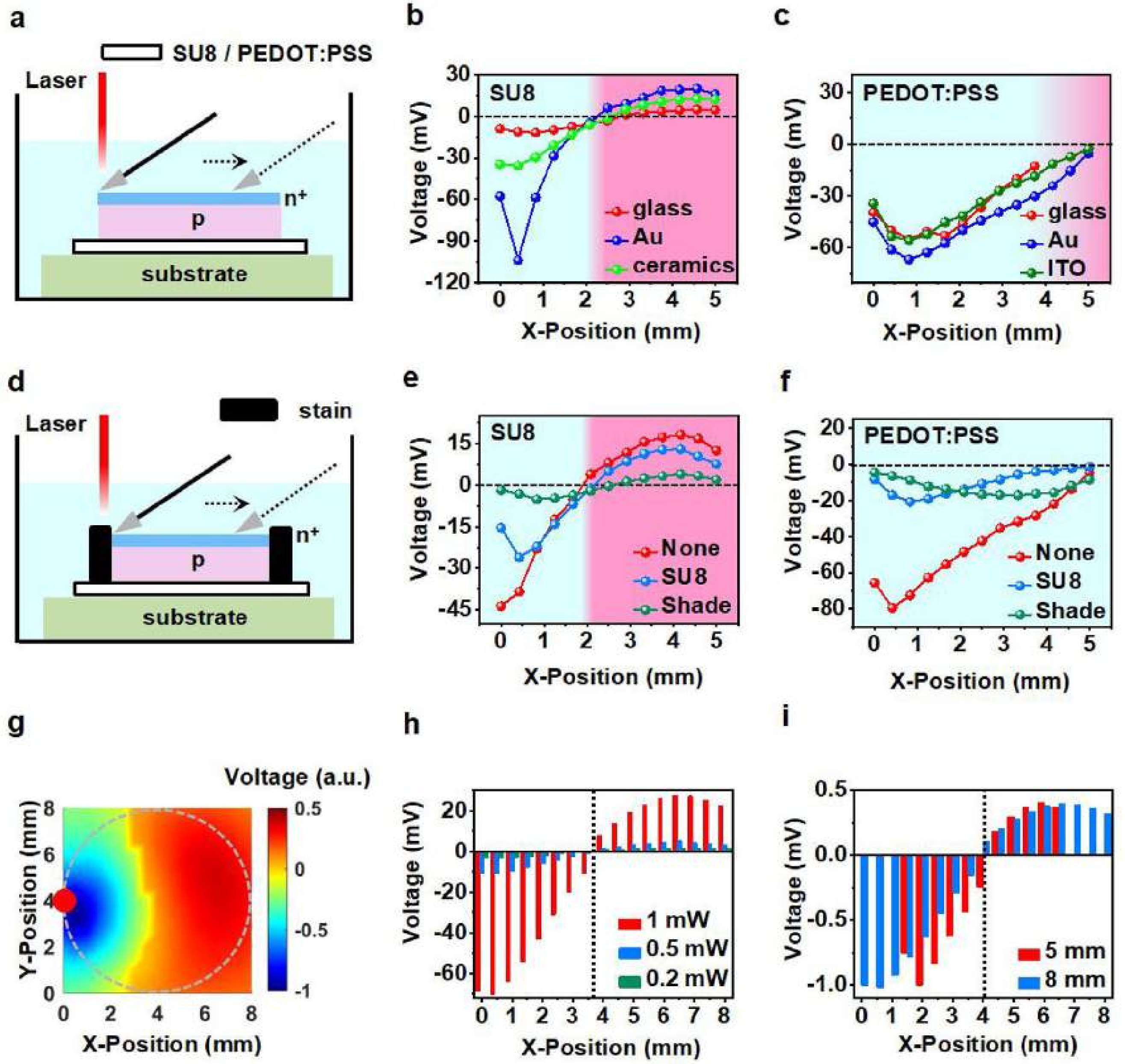

**Figure 4.** Boundary condition effects on spatial voltage distribution. The distribution of surface photovoltage peaks on pn$^+$ silicon film (5 mm diameter, 25 µm thickness, $1 \times 10^{15}$ ions cm$^{-2}$ implantation dose) under three cases: 1) Adhesion solutions: SU8 versus PEDOT: PSS. 2) Substrates: glass, Au, ceramics, and ITO. 3) Boundary conditions. a) Schematic of patch-clamp testing for a pn$^+$ sample on SU8-adhered glass substrate in PBS. b) Surface voltage variation versus distance from irradiation center for samples with SU8 adhesive on different substrates (glass, Au, ceramic). c) Surface voltage variation versus distance from irradiation center for samples with PEDOT: PSS adhesive on different substrates (glass, Au, ITO). d) Schematic of patch-clamp testing for a pn$^+$ sample in PBS with SU8 sidewall barrier and glass/SU8 substrate. e) Surface voltage versus distance from irradiation center for SU8-adhered samples with different sidewall barriers (none, transparent SU8, light-blocking SU8). f) Surface voltage versus distance from irradiation center for PEDOT: PSS-adhered samples with different sidewall barriers (none, transparent SU8, light-blocking SU8). g) Voltage distribution heatmap for an 8 mm diameter pn$^+$ sample on SU8-adhered glass. h) Central *X*-axis voltage profiles for 5 and 8 mm diameter samples at different laser intensities (0.2–1 mW). i) *X*-axis voltage distribution comparison for 5 and 8 mm samples under edge irradiation.

In conclusion, the adhesive solution critically determines the spatial voltage distribution observed in the heatmaps. Notably, the electrical and optical characteristics of the material in direct contact with the underside of the Si membrane are key to this behavior. The heatmaps for all six tested configurations are provided in Appendix Figure S3 (Supporting Information). Additionally, the dynamic changes in voltage distribution upon laser activation and deactivation—under conditions where the silicon membrane functions as either a conductive or non-conductive medium—are shown in Movies S1,S2 (Supporting Information).

Analysis of Figure 4b,c reveals that the location of peak voltage does not coincide with the center of laser illumination, diverging from theoretical expectations. We propose a plausible explanation: the glass electrode partially obstructs incident light. When the red laser beam is aligned vertically with the tip of the glass electrode, the electrode casts a shadow that attenuates the light intensity reaching the Si membrane directly beneath it. As a result, the voltage response in this region is lower than in surrounding areas, where the membrane is more fully exposed to light.

To minimize interference from ion exchange between the Si membrane's lateral edges and the surrounding solution—as well as to suppress photogalvanic effects caused by lateral light exposure—we varied the light intensity during measurements. We then compared the heatmaps of voltage peak values across the interfaces between the sealed boundaries (hereafter referred to as "seals") and the solution under various substrate conditions. We also analyzed how these voltage peaks varied along the $x$-axis. To investigate the impact of boundary conditions, we designed two distinct seal configurations. In the first, we used SU8, a non-conductive yet optically transparent photoresist, as the barrier layer. In the second, we incorporated a black dye into the SU8 to create a boundary that blocks light while remaining electrically insulating (Figure 4d).

To represent non-conductive and conductive substrate conditions, we selected SU8-glass and PEDOT: PSS-Au, respectively. A 635 nm red laser with a 200 µm spot diameter was used to irradiate the center of the left edge of the Si membrane. The membrane, 25 µm thick and of the pn$^+$ type, was measured at the injection surface (n$^+$ side) to monitor the voltage response. Figure 4e presents the voltage distribution for the SU8-glass substrate under three sealing conditions: unsealed, sealed with transparent SU8, and sealed with light-blocking SU8. In all cases, the illuminated region exhibited a negative voltage, while the dark region showed a positive voltage. The point of voltage polarity reversal remained fixed across all sealing types. In contrast, Figure 4f shows the variation in peak voltage values along the $x$-axis when the substrate is PEDOT: PSS-Au, again under unsealed, SU8-sealed, and light-blocking SU8-sealed conditions. The corresponding heatmap is shown in Figure S4 (Supporting Information). Across all three configurations, the voltage profiles remained similar, and no polarity reversal was observed. This consistency indicates that changes in boundary sealing do not affect the polarity behavior, confirming that the substrate material itself is the dominant factor governing surface voltage distribution. Interestingly, regardless of whether the region is illuminated or in darkness, and independent of whether the substrate is conductive or non-conductive, the peak voltage values consistently shift closer to the center of the Si membrane in the following order: unsealed, sealed with SU8, and sealed with light-blocking SU8. Correspondingly, the signal amplitudes decrease in the same sequence. This pattern indicates that both ion exchange at the membrane–solution boundary and the presence or absence of light exposure significantly influence the magnitude of the surface voltage. However, these factors do not alter the occurrence or location of the voltage polarity reversal.

To further investigate what governs the reversal phenomenon, we examined whether the membrane's size plays a role. For this purpose, we fabricated a pn$^+$ Si membrane with a diameter of 8 mm while maintaining the same 25 µm thickness as the previously studied 5 mm membrane. A 2D spatial heatmap was then generated for the larger membrane, and its distribution was compared to that of the 5 mm Si membrane (see Figure S5, Supporting Information). The results show that the voltage signal remains negative in the illuminated region and positive in the non-illuminated region of the Si membrane (Figure 4g). We plotted the peak voltage values along the central $x$-axis at the moment of laser activation for both the 8 and 5 mm diameter membranes on a single graph for direct comparison (Figure 4i). The data sets were centrally aligned to highlight differences in voltage distribution. Remarkably, regardless of whether the membrane diameter is 5 or 8 mm, and with the laser spot size held constant, a voltage polarity reversal consistently occurs at the center of the membrane. This observation confirms that the reversal is not size-dependent, but rather results from the lateral migration of photoinduced charge carriers within the Si membrane as they move to restore electrostatic equilibrium.

We further investigated this behavior by varying the light intensity during irradiation of the 8 mm-diameter Si membrane (Figure 4h: 0.2, 0.5, and 1 mW). Despite changes in intensity, the overall voltage distribution and the reversal position remained unchanged. At lower intensities (0.2 and 0.5 mW), the voltage signal was weak, but a substantial increase in amplitude was observed when the intensity was raised to 1 mW.

### 2.5. Geometry-Dependent Voltage Distribution in Si Membranes

Building on observations from 8 mm-diameter membranes, we systematically examined how membrane geometry influences charge redistribution. We studied 25 µm-thick pn$^+$ type silicon membranes bonded to insulating SU8-glass substrates across four geometries: circular (5 mm diameter, **Figure** 5a-i), grid ($3 \times 2$ mm$^2$, Figure 5b-i), square (2 mm edge length, Figure 5c-i), and ribbon ($5 \times 1$ mm$^2$, Figure 5d-i). Illumination at the n$^+$ side edge using a 635 nm laser with a 200 µm spot size consistently induced voltage polarity reversals between illuminated and dark regions in all insulating samples.

The circular and grid-shaped membranes (Figure 5a-ii,b-ii) exhibited symmetric inversion boundaries centered on their geometric midpoints. Notably, grid-like voltage contours appeared along these polarity transition zones, confirming that membrane morphology dictates the local electric field distribution. By contrast, square and ribbon membranes (Figure 5c-ii,d-ii) showed axis-dependent responses. Illumination predominantly along the $x$-axis suppressed polarity reversal when the entire area was exposed. However, the ribbon's elongation along the $y$-axis facilitated inversion through lateral charge migration confined near the edges. These results demonstrate that the location and occurrence of voltage polarity inversion depend on charge confinement imposed by the membrane boundaries, rather than on the membrane's absolute size. While increasing laser intensity raised signal amplitude, it did not affect the threshold for inversion, indicating that carrier concentration gradients—rather than photon flux—govern the polarity reversal. Together, these findings highlight the critical influence of membrane geometry and charge dynamics in controlling voltage inversion in these silicon membrane systems.

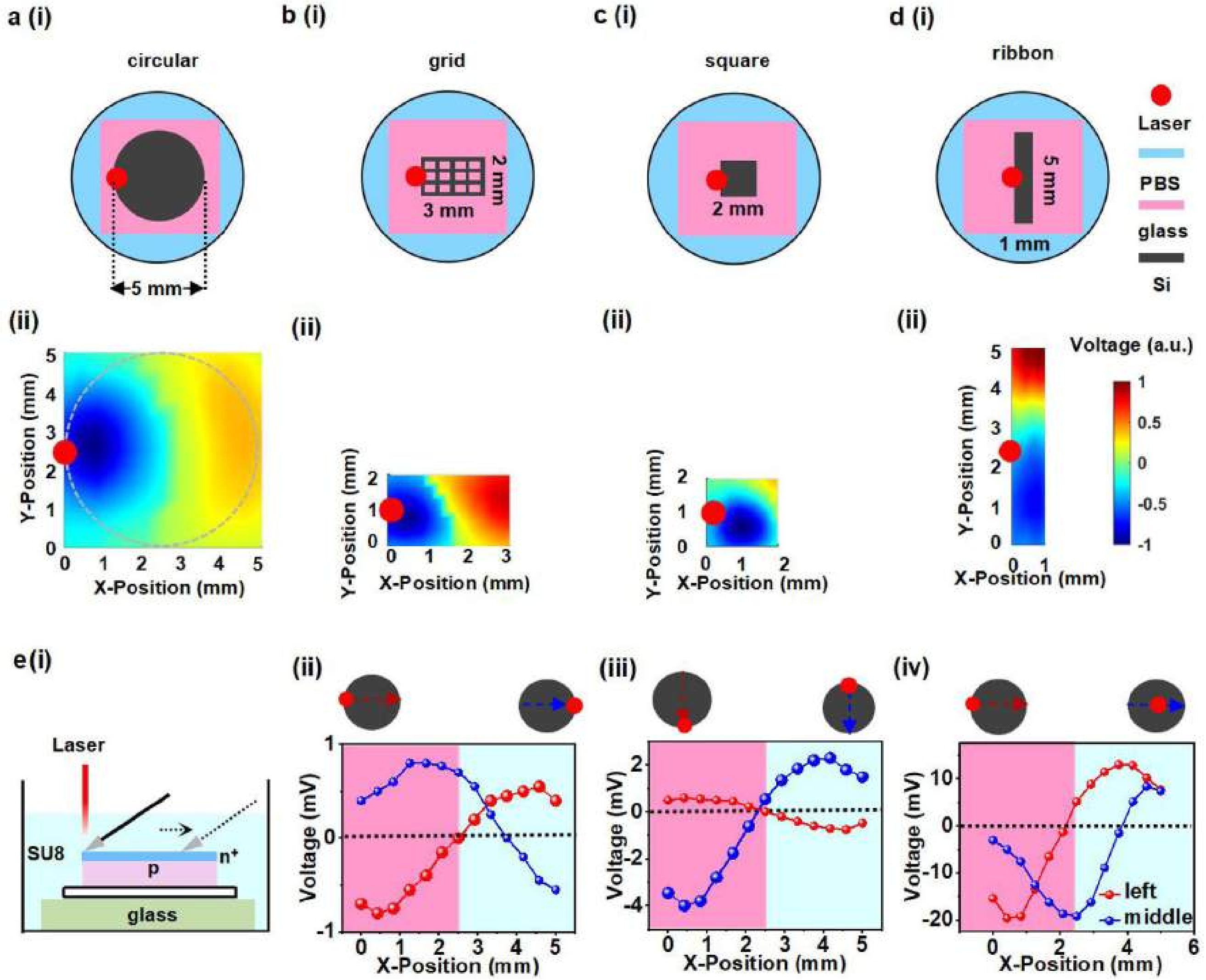

**Figure 5.** Geometry-dependent voltage distribution in silicon membranes. a) Circular film (5 mm diameter): i) schematic and ii) voltage peak heatmap. b) Mesh film (3 × 2 mm$^2$): i) schematic and ii) voltage peak heatmap. c) Square film (2 mm side length): i) schematic and ii) voltage peak heatmap. d) Strip film (5.4 × 1 mm$^2$): i) schematic and ii) voltage peak heatmap. e) Position-dependent voltage measurements in silicon membranes. Experimental design: i) Schematic of glass electrode movement relative to laser spot position. Voltage profiles during electrode scans: ii) Left-to-right scan with edge illumination (left/right edges). iii) Top-to-bottom scan with edge illumination (upper/lower edges). iv) Left-to-right scan with illumination (left/center).

To eliminate positional artifacts from the recording site and the patch clamp ground wire in the solution, we varied both the illumination location and the electrode's scanning direction during measurements. Specifically, for the Si membrane bonded with SU8 on a glass substrate (as in the prior experiment), we recorded the peak voltage at the moment the light switched on. We also measured voltage changes along both the $x$- and $y$-axes of the membrane.

Figure 5e-i shows that when illumination occurs on the membrane's left side and recording begins from the left along the $x$-axis, the voltage signal initially registers negative values before switching to positive, with polarity reversal near the membrane center. Conversely, when illumination is applied to the right side (Figure 5e-ii) while recording still starts from the left, the voltage signal initially appears positive then shifts negative. This pattern demonstrates mirror-symmetric voltage inversion across the membrane's geometric center during lateral illumination along both the $x$- and $y$-axes.

Figure 5e-iii,iv display the voltage distribution when the illumination points are positioned above and below the circular Si film, respectively, with data collection starting from the upper section of the $Y$-axis. These images show that the illuminated regions exhibit negative voltages, while the central area undergoes polarity inversion, and the unilluminated (dark) regions display positive voltages. This voltage distribution forms an almost symmetrical pattern. These results demonstrate that the voltage reversal observed in the circular Si film exhibits mirror symmetry, with the film's center serving as the axis of symmetry. The intrinsic rotational symmetry of the circular Si structure governs the symmetry of lateral charge migration pathways. Changing the illumination position produces only a spatial mirror inversion of the voltage profile; the overall distribution pattern remains unchanged.

In contrast, when the illumination point is positioned at the center of the circular film and recording begins from the left side of the *X*-axis, the voltage signal reverses at ≈4 mm. Interestingly, the voltage changes more sharply on the reversed side than on the non-reversed side. This asymmetry suggests that central illumination drives isotropic carrier diffusion outward from the center. However, the finite physical boundaries of the Si film constrain the outward spread of charges, leading to a pronounced local increase in the carrier concentration gradient.

### 2.6. Modulation of Sciatic Nerve Activity

Integrating conductive substrates effectively suppresses the formation of reverse electric fields while enhancing the photoelectric performance of thin-film Si. We first conducted in vivo experiments to evaluate neural modulation of the sciatic nerves in Sprague–Dawley (SD) rats. These studies employed Si thin-film electrodes fabricated on both non-conductive and conductive substrates. To quantify stimulation efficiency, we simultaneously recorded compound muscle action voltages (CMAPs) through implanted electrodes and monitored limb displacement using high-speed videography (**Figure 6**a). Additional details of the high-speed imaging setup are provided in Movie S3 (Supporting Information). Device fabrication involved transferring Si membranes onto two substrate types: polydimethylsiloxane (PDMS) films (0.5 mm thick) for non-conductive electrodes, and gold-patterned PDMS with stripe-shaped metallic interconnects for conductive electrodes (Figure 6b,c). The submillimeter-scale PDMS substrate provided excellent conformal contact with exposed neural tissue, eliminating the need for external fixation (Figure 6b). A schematic diagram of the setup for electromyographic signal recording appears in Figure S6 (Supporting Information).

We used a 635 nm laser (10 Hz repetition rate, 100 ms pulse width, 2 mm spot size) to uniformly photostimulate 5 mm-diameter Si electrodes. At an illumination intensity of 8 mW mm$^{-2}$, non-conductive substrates failed to evoke measurable neural responses, with CMAP amplitudes remaining below 0.1 mV (Figure 6d). In contrast, conductive substrates produced strong CMAP responses reaching up to 8 mV (Figure 6e). Additional CMAP signals generated by conductive substrates under varying light intensities are presented in Figure S7 (Supporting Information). The stimulus-response curve demonstrated clear intensity dependence, with CMAP amplitude increasing proportionally with illumination strength (Figure 6f). Notably, transient CMAP signals appeared at both the onset and offset of illumination (Figure 6g). Quantitative kinematic analysis revealed distinct motion patterns: light onset induced ≈10° of plantarflexion (Figure 6h), while light offset triggered 15° of dorsiflexion (Figure 6i), resulting in a combined angular displacement of 25°, closely resembling the biomechanics of natural bipedal gait (Movie S4, Supporting Information). This phenomenon may have caused by rebound excitation. When the light intensity is high enough, at the moment of light activation, the voltage signal stimulates the sciatic nerve, inducing depolarization of the sciatic nerve signals. This leads to neuronal excitation targeting the plantarflexor muscles, resulting in plantarflexion. At the moment of light deactivation, a reverse capacitive current is generated, causing hyperpolarization of the sciatic nerve signals. This triggers rebound excitation, activating antagonistic muscle groups and leading to dorsiflexion.[42]

Previous approaches employed distinct strategies for bidirectional optogenetic control: distinct thin-film silicon diodes generating different photoelectric fields to induce depolarization and hyperpolarization,[43] or parameter-modulated photostimulation using brief, high-intensity pulses (exploiting photothermal/photo-capacitive effects) for excitation and sustained low-intensity irradiation (utilizing diffusion-limited carrier dynamics) for inhibition.[44] In contrast, our observed bidirectional modulation emerges from the dual-phase capacitive voltage induces dual stimulations of the sciatic nerve, and the second stimulation induced rebound excitation, resulting in an antagonistic motor outcome. This bidirectional neuromodulation capability offers significant potential for restoring locomotor function in spinal cord injury models. By alternating photostimulation, it may be possible to emulate the coordinated activity of agonist and antagonist muscle groups essential for walking. These results provide a promising framework for developing optoelectronic neural interfaces with clinical relevance in neuroprosthetic applications.

## 3. Discussion

In this study, we systematically investigated the optoelectronic response of pn junction diodes (np$^+$ and pn$^+$ type Si films) fabricated from thin-film single-crystal Si in a PBS buffer solution. Our focus centered on characterizing the surface voltage distribution of the Si film under illumination and elucidating the underlying mechanisms governing its behavior. Through a combination of systematic experiments and theoretical modeling, we uncovered the complex optoelectronic response of Si-based devices operating in biological environments. At the core of this mechanism is the dynamic interplay between two competing processes: longitudinal separation of photogenerated carriers driven by the built-in electric field of the pn junction, and lateral carrier migration constrained by charge conservation. This competition plays a critical role in determining device performance at biological interfaces. Notably, we found that employing conductive substrates significantly improves electrical stimulation efficiency by suppressing lateral charge migration, although this enhancement comes with a trade-off in spatial resolution. Additionally, we examined how multiple factors—including substrate material, the physicochemical properties of the interfacing solution, and the geometric configuration of the Si film—affect the spatial distribution of surface voltage. These findings provide important design principles for optimizing Si-based optoelectronic devices for bioelectronic interface applications.

While adhesive bonding (e.g., PEDOT: PSS) facilitates uniform carrier diffusion and enhances lateral transport through operational simplicity, it imposes three fundamental constraints: i) increased interfacial resistance, ii) uncontrolled layer thickness, and iii) electrolyte penetration through microporous networks. For optimized device performance, direct backside deposition (e.g., Au, ITO) provides atomic-scale interfacial control—reducing resistance, preserving intrinsic silicon thickness, and eliminating porous degradation pathways.[45]

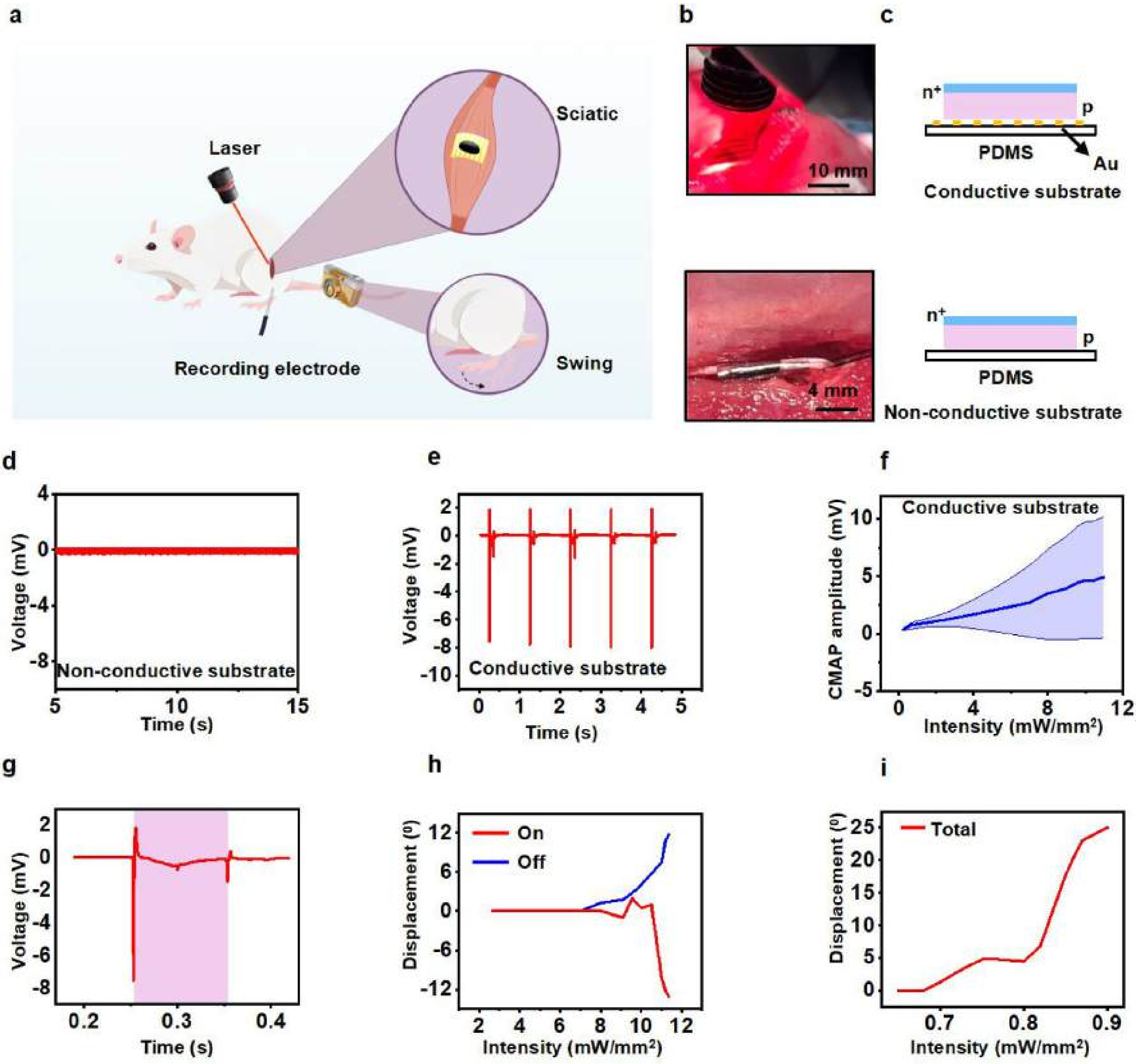

**Figure 6.** Modulation of sciatic nerve activity. a) Experimental setup: silicon membrane with conductive substrate attached to rat sciatic nerve, with EMG electrodes in the gastrocnemius muscle for CMAP recording. b) Implantation photographs: conductive substrate (top) and non-conductive substrate (bottom) on the sciatic nerve. c) Substrate schematics: PDMS-supported silicon membrane with strip-shaped Au (conductive, top) and without metal (non-conductive, bottom). d) No detectable CMAP signal at 8 mW mm$^{-2}$ illumination with non-conductive substrate. e) Clear CMAP signal at the same intensity (8 mW mm$^{-2}$) with a conductive substrate. f) CMAP signal amplitude increases with light intensity. g) CMAP signal from single stimulation using conductive-substrate silicon membrane. h) Bidirectional thigh movement upon light activation/deactivation, with amplitude dependent on light intensity. i) Total thigh displacement versus laser intensity.

Future research should advance along several key directions. i) By integrating semiconductor energy band theory with double-layer dynamics and ion transport equations, it will be possible to develop a multiscale, coupled physical model capable of quantitatively predicting voltage distributions under diverse interface conditions. ii) Engineering the substrate architecture or introducing microstructural features on the Si film surface—such as patterned substrates or nanopore arrays—can tailor charge extraction pathways and ion diffusion channels. This approach could enable the coordinated optimization of both voltage amplitude and spatial precision. iii) The sciatic nerve experiment in this study serves as a preliminary demonstration, providing design principles for scenarios requiring higher-precision stimulation across substrate selection, material properties, and optimization of spatial stimulation distribution. For example, in photovoltaic retinal research,[24,46,47] precise regional voltage modulation allows silicon membranes to closely replicate photoreceptor cell responses. Simultaneously, controlling voltage gradients can

**Table 1.** Estimation Table of Equivalent Circuit Components.

| Element | Formula | Estimated Value |
|---|---|---|
| $C_{sc}$ | $C_{sc} = \frac{\varepsilon_{Si} \times \varepsilon_0 \times A}{W_{dep}}$ | 254.8 nF |
| $C_H$ | $C_H = \frac{\varepsilon_H \times \varepsilon_0 \times A}{d_H}$ | 0.22 μF |
| $C_{dl}$ | $\frac{1}{C_{dl}} = \frac{1}{C_{sc}} + \frac{1}{C_H}$ | 118 nF |
| $R_{faraday}$ | $R_{faraday} \approx \frac{d\eta}{di_{\eta=0}} \approx \frac{RT}{nFj_0A}$ | 128 MΩ |
| $R_{Si}$ | $R_{Si} = \frac{\rho_{Si} \times L}{A}$ | 0.127 Ω |

improve the overall efficiency of photovoltaic materials, enhancing image resolution and contrast for retinal prosthetic applications.

In summary, this study establishes a crucial experimental foundation for advancing interface engineering in Si-based bioelectronic devices. These findings are particularly relevant for neural interfaces and optically controlled electrical stimulation technologies, both of which have promising applications in neuro-engineering and healthcare. Future efforts can further enhance device performance through interdisciplinary approaches. Specifically, rationally designing substrate conductivity and device geometry will enable precise regulation of photogenerated voltages, supporting the development of next-generation programmable optoelectronic neural interfaces and accelerating their translation into clinical applications.

## 4. Experimental Section

*Fabrication of Silicon Film Samples*: The SOI substrate underwent sequential cleaning in $NH_4OH$: $H_2O_2$:$H_2O$ (1:1:5) at 80 °C (10 min), diluted HF (1:50, 20 s), and HCl: $H_2O_2$:$H_2O$ (1:1:6) at 80 °C (10 min), with DI water rinsing between steps. Phosphorus doping was achieved via ion implantation (30 keV, 1 $e^{15}$ ions $cm^{-2}$), followed by $H_2SO_4$:$H_2O_2$ (3:1) cleaning (120 °C, 30 min) and annealing. Photolithography utilized SPR-220 for thin films (1.5–2.5 μm; spin-coated at 3000 rpm, exposed at 45 mJ $cm^{-2}$, developed in AZ developer) or AZ4620 for thick films (25 μm; 2000 rpm, 400 mJ $cm^{-2}$ exposure). Patterns were defined via SF6-based RIE (150 sccm, 80 Pa, 100 W; 240 s for 2.5 μm, 2200 s for 25 μm). The buried oxide was removed by HF etching (4 h for thin films, 8 h for thick films). Released silicon membranes were transferred onto adhesion-coated substrates (PEDOT: PSS or SU8 on Au/glass/ceramic/ITO) by thermal release tape or PDMS stamps, followed by bonding (130 °C, 30 min). Surface conductivity was enhanced by coating Au nanoparticles via 2-min treatment in $HAuCl_4 \cdot H_2O$:HF: $H_2O$ (100 μL:125 μL:5 mL) solution.

*Measurement of the Voltage Signal*: The prepared device was immersed in a PBS solution, and a standard patch clamp system was used to measure the photoresponse of the optoelectronic device. A red laser beam (635 nm laser, 10 Hz, pulse width of 10 ms, spot size of 200 micrometers) was incident on the device through an optical fiber. The voltage-clamp and current-clamp proto were controlled by an Axonpatch 200B amplifier controlled by p-Clamp software (Molecular Devices). A glass pipette filled with PBS solution (≈1 MΩ) was brought close to the surface of the device within a distance of 5–10 μm and could be freely moved in the $X$ and $Y$ directions by a micromanipulator. The voltage or current clamp (filtered at 10 kHz and sampled at 200 kHz) was used to record the transient photoresponse of the device.

*Acute Sciatic Nerve Stimulation*: All procedures related to animal research complied with the institutional guidelines of Tsinghua University. The Animal Care and Use Committee of Tsinghua University reviewed and approved the experimental protocol. All Sprague–Dawley (SD) rats were intraperitoneally injected with a 1% sodium pentobarbital solution at 0.3 ml/100 g body weight. Then, the hair on the right femur was removed. An incision was made along the midline of the skin, and the fascia between the gluteus maximus muscle and the anterior head of the biceps femoris muscle was separated with forceps to expose the sciatic nerve. The optoelectronic device was curled and connected to the sciatic nerve, and parallel recording electrodes were placed on the gastrocnemius muscle to record the CMAP. The CMAP data were collected using the RM6240E device from Chengdu Instrument Factory, and a camera recorded the movement of the right hind limb. The entire experiment was conducted in a shielded cage to block external signals.

*The Capacitive Double Layer at the Silicon–Solution Interface*: The capacitive double layer at silicon–electrolyte interfaces governs critical electrochemical processes through five key elements: space charge capacitance ($C_{sc}$), Helmholtz capacitance ($C_H$), interfacial capacitance ($C_{dl}$), Faradaic resistance $R_f$), and bulk resistance ($R_{Si}$). These components collectively dictate interfacial dynamics from picosecond charge redistribution to second-scale electrochemical reactions, with direct implications for energy and sensing technologies. The formulas and estimated values of each component are shown in **Table 1**.

i. Space charge capacitance[48] ($C_{sc}$) emerged from Fermi-level-driven band bending in silicon, where carrier redistribution (nanosecond-microsecond timescales) responded to applied bias. Its magnitude reflected doping concentration and defines operational regimes (depletion, inversion). $\epsilon_{Si} = 11.7$ for silicon, $W_{dep} \approx 8$ μm is the depletion width, and $A = 19.6$ $mm^2$ (5-mm-diameter membrane).
ii. Helmholtz capacitance[49] ($C_H$) represented the sub-nanometer ion-solvent layer at the electrode surface, exhibiting ultrafast (picosecond) polarization dynamics sensitive to interfacial chemistry. $\epsilon_H \approx 10$ for PBS, $d_H \approx 0.4$ nm.
iii. Interfacial capacitance[49] ($C_{dl}$) arised from surface states or oxide layers, displaying state-dependent kinetics (microsecond-second) that revealed surface quality and passivation effects. The total capacitance was limited by a smaller value ($C_H$) in the depleted/reversed state.
iv. Faradaic resistance[50] ($R_{faraday}$) quantified charge-transfer barriers for interfacial reactions (millisecond-second), serving as a direct probe of catalytic activity and corrosion kinetics. For $j_0 = 1$ μA $cm^{-2}$, $n = 1$, and 19.6 $mm^2$ area(5-mm-diameter membrane). At 298 K(25 °C), the thermal voltage RT/F equals 25.7 mV.
v. Bulk resistance ($R_{Si}$) provided the instantaneous ohmic baseline, enabling discrimination of interfacial phenomena from material-limited contributions. $\rho_{Si} = 10$ Ω cm, 19.6 $mm^2$ area(5-mm-diameter membrane), $L = 25$ μm.

The rise time (temporal resolution) of the voltage signal was mainly determined by the RC time constant in the circuit:

$$\tau_{interface} \approx (R_{Si} + R_{sol}) \times C_{dl} \approx 0.1s \tag{1}$$

where $R_{sol} \approx 1$ MΩ. The photo-generated charges took time to be conducted through the silicon bulk and the solution to alter the amount of charge stored on both sides of the interface. This determined the rate at which the localized interfacial potential difference establishes in illuminated or non-illuminated regions.

Faradaic process time constant $\tau_{faraday}$:

If Faradaic processes participate in charge transfer (which commonly occurs in photoelectrochemical systems), another time constant exists:

$$\tau_{faraday} \approx R_{faraday} \times C_{dl} \approx 15.1s \tag{2}$$

This time constant represented the duration required to transfer sufficient charge through electrochemical reactions to significantly alter interfacial states (such as surface state charging or changes in reactant concentration). It was typically significantly greater than $\tau_{interface}$, indicating that the charging/discharging of interfacial capacitance occurred much faster than Faradaic reactions. During the initial transient response phase (e.g., immediately after light pulse activation or deactivation), $\tau_{interface}$ tended to dominate the rapid signal variations. In steady-state or slow-varying processes, Faradaic processes and potential diffusion processes (Warburg impedance) became dominant. This was also consistent with the results obtained from the experiment.

## Supporting Information

Supporting Information is available from the Wiley Online Library or from the author.

## Acknowledgements

This work was supported by the National Natural Science Foundation of China (NSFC) (62404032, to L.L., T2425003, and 52272277, to X.S.), the STI 2030-Major Projects (2022ZD0208500).

## Conflict of Interest

The authors declare no conflict of interest.

## Author Contributions

L.L., X.S., and D.Y. developed the concepts. L.L.,Y.Z., Y.G., and X.S. performed material and device and circuit design, fabrication, and characterization. L.L., Y.W., S.W., X.G., L.Y., K.C., and X.S. designed and performed biological experiments. L.L. and X.S. wrote the paper in consultation with other authors.

## Data Availability Statement

All data needed to evaluate the conclusions in the paper are present in the main text or the supplementary materials.

## Keywords

bidirectional response, neuromodulation, Si membrane-solution interface

Received: June 30, 2025
Revised: August 1, 2025
Published online: October 15, 2025

---

[1] K. Ashkan, P. Rogers, H. Bergman, I. Ughratdar, *Nat. Rev. Neurol.* **2017**, *13*, 548.
[2] R. S. Fisher, A. L. Velasco, *Nat. Rev. Neurol.* **2014**, *10*, 261.
[3] N. Wenger, E. M. Moraud, J. Gandar, P. Musienko, M. Capogrosso, L. Baud, C. G. Le Goff, Q. Barraud, N. Pavlova, N. Dominici, I. R. Minev, L. Asboth, A. Hirsch, S. Duis, J. Kreider, A. Mortera, O. Haverbeck, S. Kraus, F. Schmitz, J. DiGiovanna, R. van den Brand, J. Bloch, P. Detemple, S. P. Lacour, E. Bézard, S. Micera, G. Courtine, *Nat. Med.* **2016**, *22*, 138.
[4] S. Rahimpour, W. Gaztanaga, A. P. Yadav, S. J. Chang, M. O. Krucoff, I. Cajigas, D. A. Turner, D. D. Wang, *Neuromodulation* **2021**, *24*, 829.
[5] U. Topalovic, S. Barclay, C. Ling, A. Alzuhair, W. Yu, V. Hokhikyan, H. Chandrakumar, D. Rozgic, W. Jiang, S. Basir-Kazeruni, S. L. Maoz, C. S. Inman, M. Stangl, J. Gill, A. Bari, A. Fallah, D. Eliashiv, N. Pouratian, I. Fried, N. Suthana, D. Markovic, *Nat. Neurosci.* **2023**, *26*, 517.
[6] A. Zhou, S. R. Santacruz, B. C. Johnson, G. Alexandrov, A. Moin, F. L. Burghardt, J. M. Rabaey, J. M. Carmena, R. Muller, *Nat. Biomed. Eng.* **2019**, *3*, 15.
[7] K. W. Scangos, A. N. Khambhati, P. M. Daly, G. S. Makhoul, L. P. Sugrue, H. Zamanian, T. X. Liu, V. R. Rao, K. K. Sellers, H. E. Dawes, P. A. Starr, A. D. Krystal, E. F. Chang, *Nat. Med.* **2021**, *27*, 1696.
[8] I. O. Bergfeld, M. Mantione, M. L. C. Hoogendoorn, H. G. Ruhé, P. Notten, J. van Laarhoven, I. Visser, M. Figee, B. P. de Kwaasteniet, F. Horst, A. H. Schene, P. van den Munckhof, G. Beute, R. Schuurman, D. Denys, *JAMA Psychiatry* **2016**, *73*, 456.
[9] R.o' Gilron, S. Little, R. Perrone, R. Wilt, C. de Hemptinne, M. S. Yaroshinsky, C. A. Racine, S. S. Wang, J. L. Ostrem, P. S. Larson, D. D. Wang, N. B. Galifianakis, I. O. Bledsoe, M. San Luciano, H. E. Dawes, G. A. Worrell, V. Kremen, D. A. Borton, T. Denison, P. A. Starr, *Nat. Biotechnol.* **2021**, *39*, 1078.
[10] K. Zhou, W. Wei, D. Yang, H. Zhang, W. Yang, Y. Zhang, Y. Nie, M. Hao, P. Wang, H. Ruan, T. Zhang, S. Wang, Y. Liu, *Nat. Commun.* **2024**, *15*, 619.
[11] O. Yizhar, L. E. Fenno, T. J. Davidson, M. Mogri, K. Deisseroth, *Neuron* **2011**, *71*, 9.
[12] K. M. Tye, K. Deisseroth, *Nat. Rev. Neurosci.* **2012**, *13*, 251.
[13] E. S. Boyden, F. Zhang, E. Bamberg, G. Nagel, K. Deisseroth, *Nat. Neurosci.* **2005**, *8*, 1263.
[14] R. C. Wykes, D. M. Kullmann, I. Pavlov, V. Magloire, *J. Neurosci. Methods* **2016**, *260*, 215.
[15] D. M. Kullmann, S. Schorge, M. C. Walker, R. C. Wykes, *Nat. Rev. Neurol.* **2014**, *10*, 300.
[16] M. Silverå Ejneby, M. Jakešová, J. J. Ferrero, L. Migliaccio, I. Sahalianov, Z. Zhao, M. Berggren, D. Khodagholy, V. Đerek, J. N. Gelinas, E. D. Glowacki, *Nat. Biomed. Eng.* **2021**, *6*, 741.
[17] S. M. Won, E. Song, J. T. Reeder, J. A. Rogers, *Cell* **2020**, *181*, 115.
[18] Y. Jiang, X. Li, B. Liu, J. Yi, Y. Fang, F. Shi, X. Gao, E. Sudzilovsky, R. Parameswaran, K. Koehler, V. Nair, J. Yue, K. H. Guo, Y. Fang, H. M. Tsai, G. Freyermuth, R. C. S. Wong, C. M. Kao, C. T. Chen, A. W. Nicholls, X. Wu, G. M. G. Shepherd, B. Tian, *Nat. Biomed. Eng.* **2018**, *2*, 508.
[19] P. Li, J. Zhang, H. Hayashi, J. Yue, W. Li, C. Yang, C. Sun, J. Shi, J. Huberman-Shlaes, N. Hibino, B. Tian, *Nature* **2024**, *626*, 990.
[20] Y. Zhang, E. Rytkin, L. Zeng, J. U.k Kim, L. Tang, H. Zhang, A. Mikhailov, K. Zhao, Y. Wang, L.i Ding, X. Lu, A. Lantsova, E. Aprea, G. Jiang, S. Li, S. G.i Seo, T. Wang, J. Wang, J. Liu, J. Gu, F. Liu, K. Bailey, Y. F. L. Li, A. Burrell, A. Pfenniger, A. Ardashev, T. Yang, N. Liu, Z. Lv, N. S. Purwanto, et al., *Nature* **2025**, *640*, 77.
[21] A. Prominski, J. Shi, P. Li, J. Yue, Y. Lin, J. Park, B. Tian, M. Y. Rotenberg, *Nat. Mater.* **2022**, *21*, 647.
[22] Y. Huang, Y. Cui, H. Deng, J. Wang, R. Hong, S. Hu, H. Hou, Y. Dong, H. Wang, J. Chen, L. Li, Y. Xie, P. Sun, X. Fu, L. Yin, W. Xiong, S.-H. Shi, M. Luo, S. Wang, X. Li, X. Sheng, *Nat. Biomed. Eng.* **2023**, *7*, 486.
[23] D. Ghezzi, M. R. Antognazza, R. Maccarone, S. Bellani, E. Lanzarini, N. Martino, M. Mete, G. Pertile, S. Bisti, G. Lanzani, F. Benfenati, *Nat. Photonics* **2013**, *7*, 400.
[24] J. F. Maya-Vetencourt, D. Ghezzi, M. R. Antognazza, E. Colombo, M. Mete, P. Feyen, A. Desii, A. Buschiazzo, M. Di Paolo, S. Di Marco, F. Ticconi, L. Emionite, D. Shmal, C. Marini, I. Donelli, G. Freddi, R. Maccarone, S. Bisti, G. Sambuceti, G. Pertile, G. Lanzani, F. Benfenati, *Nat. Mater.* **2017**, *16*, 681.
[25] J. A. Frank, M.-J. Antonini, P. Anikeeva, *Nat. Biotechnol.* **2019**, *37*, 1013.
[26] C. Yang, Z. Cheng, P. Li, B. Tian, *Acc. Chem. Res.* **2024**, *57*, 1398.
[27] P. Sun, C. Li, C. Yang, M. Sun, H. Hou, Y. Guan, J. Chen, S. Liu, K. Chen, Y. Ma, Y. Huang, X. Li, H. Wang, L. Wang, S. Chen, H. Cheng, W. Xiong, X. Sheng, M. Zhang, J. Peng, S. Wang, Y. Wang, L. Yin, *Nat. Commun.* **2024**, *15*, 4721.
[28] Z. Ye, A. Prominski, B. Tian, G. Galli, *Proc. Natl. Acad. Sci. U.S.A.* **2021**, *118*, 2114929118.

[29] J. Li, Y. Long, Z. Hu, J. Niu, T. Xu, M. Yu, B. Li, X. Li, J. Zhou, Y. Liu, *Nat. Commun.* **2021**, *12*, 4998.
[30] Z. Liao, J. Li, Y. Long, H. Sheng, X. Wang, X. Li, W. Guo, J. Yin, *ACS Appl. Mater. Interfaces* **2023**, *15*, 57812.
[31] L. Fabbri, L. Migliaccio, A. Širvinskytė, G. Rizzi, L. Bondi, C. Tamarozzi, S. A. L. Weber, B. Fraboni, E. D. Glowacki, T. Cramer, *Adv. Mater. Interfaces* **2025**, *12*, 2400822.
[32] N. A. L. Chenais, M. J. I. Airaghi Leccardi, D. Ghezzi, *Commun. Mater.* **2021**, *2*, 28.
[33] J. Chen, J. Xu, S. Shi, R. Cao, D. Liu, Y. Bu, P. Yang, J. Xu, X. Zhang, L. Li, *ACS Appl. Mater. Interfaces* **2020**, *12*, 23145.
[34] C. He, D. Guo, K. Chen, S. Wang, J. Shen, N. Zhao, A. Liu, Y. Zheng, P. Li, Z. Wu, C. Li, F. Wu, W. Tang, *ACS Appl. Nano Mater.* **2019**, *2*, 4095.
[35] S. Zhang, A. Hu, Q. Liu, L.i Xu, X. Ren, B.o Wang, Y. Ren, W. Liu, X. Zhou, S. Chen, X. Guo, *Adv. Electron. Mater.* **2023**, *9*, 2300243.
[36] D. Wang, X. Liu, Y. Kang, X. Wang, Y. Wu, S. Fang, H. Yu, M. H. Memon, H. Zhang, W. Hu, Z. Mi, L. Fu, H. Sun, S. Long, *Nat. Electron.* **2021**, *4*, 645.
[37] S. M. Sze, K. K. Ng, *Wiley-Interscience Publication*, Hoboken, USA, **2006**.
[38] Y. Jiang, R. Parameswaran, X. Li, J. L. Carvalho-de-Souza, X. Gao, L. Meng, F. Bezanilla, G. M. G. Shepherd, B. Tian, *Nat. Protoc.* **2019**, *14*, 1339.
[39] F. H. L. Koppens, T. Mueller, P. Avouris, A. C. Ferrari, M. S. Vitiello, M. Polini, *Nat. Nanotechnol.* **2014**, *9*, 780.
[40] B. Tian, C. Lieber, *Chem. Rev.* **2019**, *119*, 9136.
[41] P. Li, J. Zhang, H. Hayashi, J. Yue, W. Li, *Nature* **2024**, *626*, 990.
[42] M. Kano, U. Rexhausen, J. Dreessen, A. Konnerth, *Nature* **1992**, *356*, 601.
[43] Y. Huang, Y. Cui, H. Deng, J. Wang, R. Hong, S. Hu, H. Hou, Y. Dong, H. Wang, J. Chen, L. Li, Y. Xie, P. Sun, X. Fu, L. Yin, W. Xiong, S. H. Shi, M. Luo, S. Wang, X. Li, X. Sheng, *Nat. Biomed. Eng.* **2023**, *7*, 486.
[44] X. Fu, Z. Hu, W. Li, L. Ma, J. Chen, M. Liu, S. Hu, H. Wang, Y. Huang, G. Tang, B. Zhang, X. Cai, Y. Wang, L. Li, J. Ma, S. Shi, L. Yin, H. Zhang, X. Li, X. Sheng, *Proc. Natl. Acad. Sci. U. S. A.* **2024**, *30*, 121.
[45] Z. He, R. Yu, Y. Dong, R. Wang, Y. Zhang, Z. ’. Tan, *Nat. Commun.* **2025**, *16*, 1773.
[46] Y. Wang, L. Yin, S. Huang, R. Xiao, Y. Zhang, *Nano Lett.* **2023**, *23*, 8460.
[47] N. Chenais, M. Airaghi Leccardi, D. Ghezzi, *Commun. Mater.* **2021**, *2*, 28.
[48] S. S. Li, *Semiconductor Physical Electronics*, Springer, Berlin, Germany, **2010**.
[49] J. Le, J. Cheng, *Curr. Opin. Electrochem.* **2021**, *27*, 100693.
[50] L. Baggetto, R. A. H. Niessen, P. H. L. Notten, *Electrochim. Acta.* **2009**, *54*, 5937.

# Supporting Information

## Figure S1

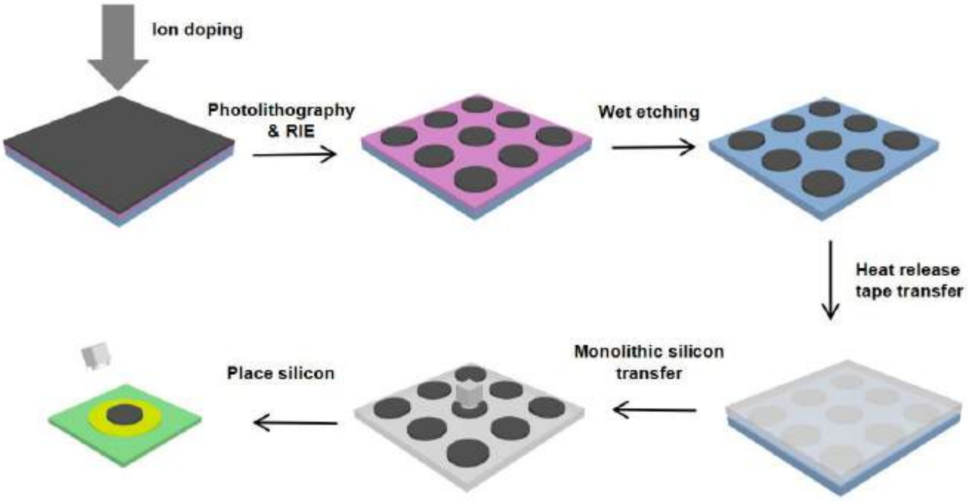

**Figure S1. Fabrication process for thin-film silicon devices.** 1) Pattern ion-doped np$^+$ silicon into 5 mm diameter circles via photolithography and reactive ion etching. 2) Release films from the substrate using HF wet etching and thermal tape liftoff. 3) Transfer to target substrates (PEDOT: PSS or SU8-coated) using PDMS stamps.

# Figure S2

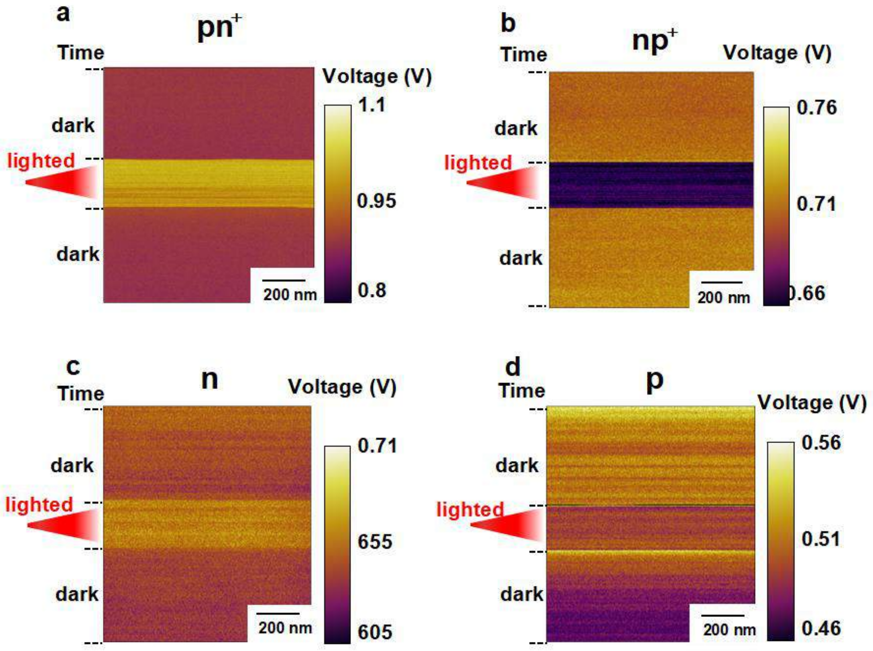

**Figure S2. Surface voltage mapping under illumination (1 µm scan area).** a) Voltage inversion occurs uniformly in both dark and illuminated regions. b) Uniform voltage decrease is observed across all regions. c) Consistent voltage increase in dark and illuminated areas. d) Voltage reduction occurs uniformly regardless of illumination.

# Figure S3

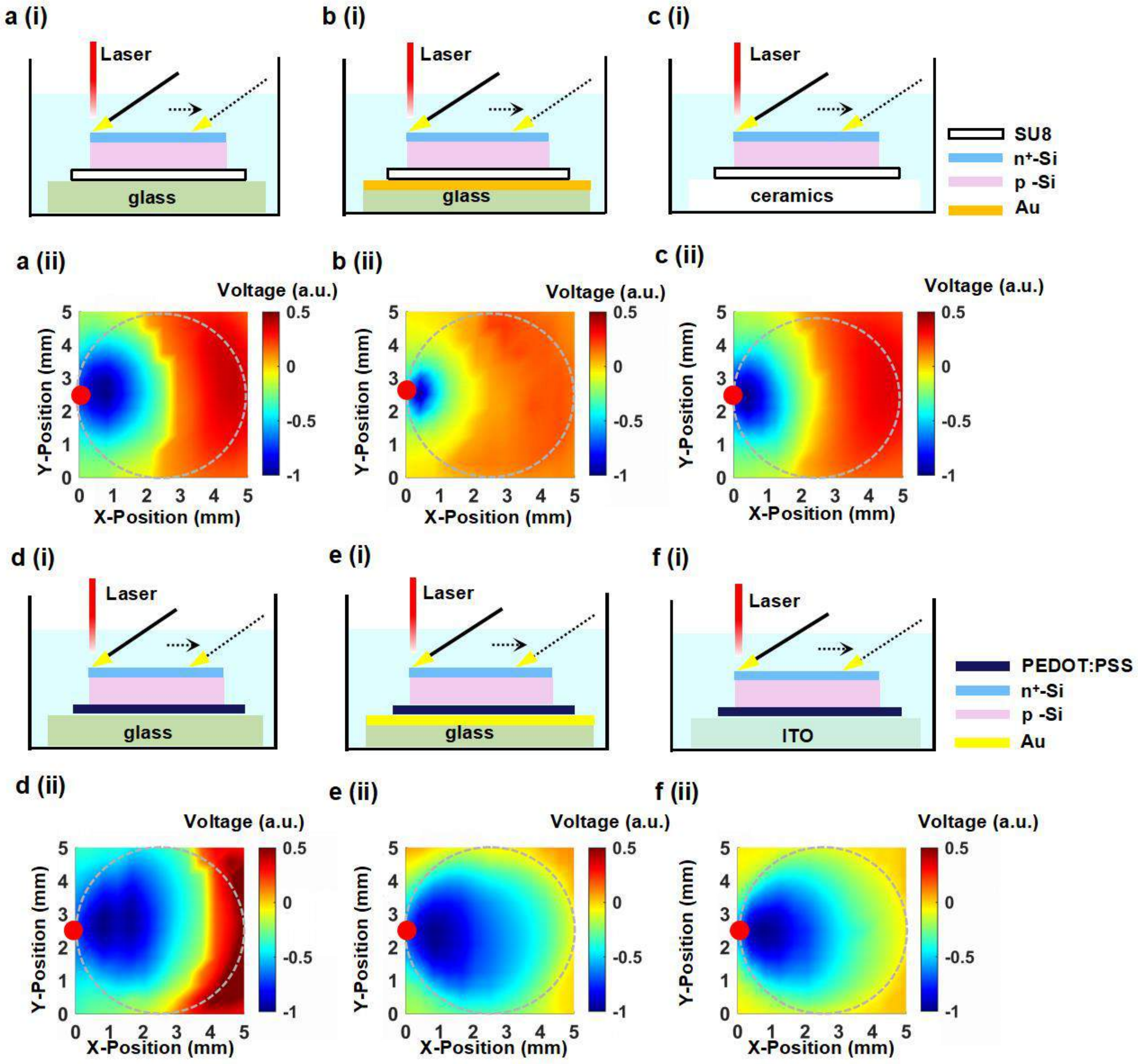

**Figure S3. Substrate-dependent surface voltage variations in silicon films.** a) Glass/SU8 configuration: i) schematic and ii) voltage peak heatmap. b) Au/SU8 configuration: i) schematic and ii) voltage peak heatmap. c) Ceramic/SU8 configuration: i) schematic and ii) voltage peak heatmap. d) Glass/PEDOT:PSS configuration: i) schematic and ii) voltage peak heatmap. e) Au/PEDOT:PSS configuration: i) schematic and ii) voltage peak heatmap. f) ITO/PEDOT:PSS configuration: i) schematic and ii) voltage peak heatmap.

# Figure S4

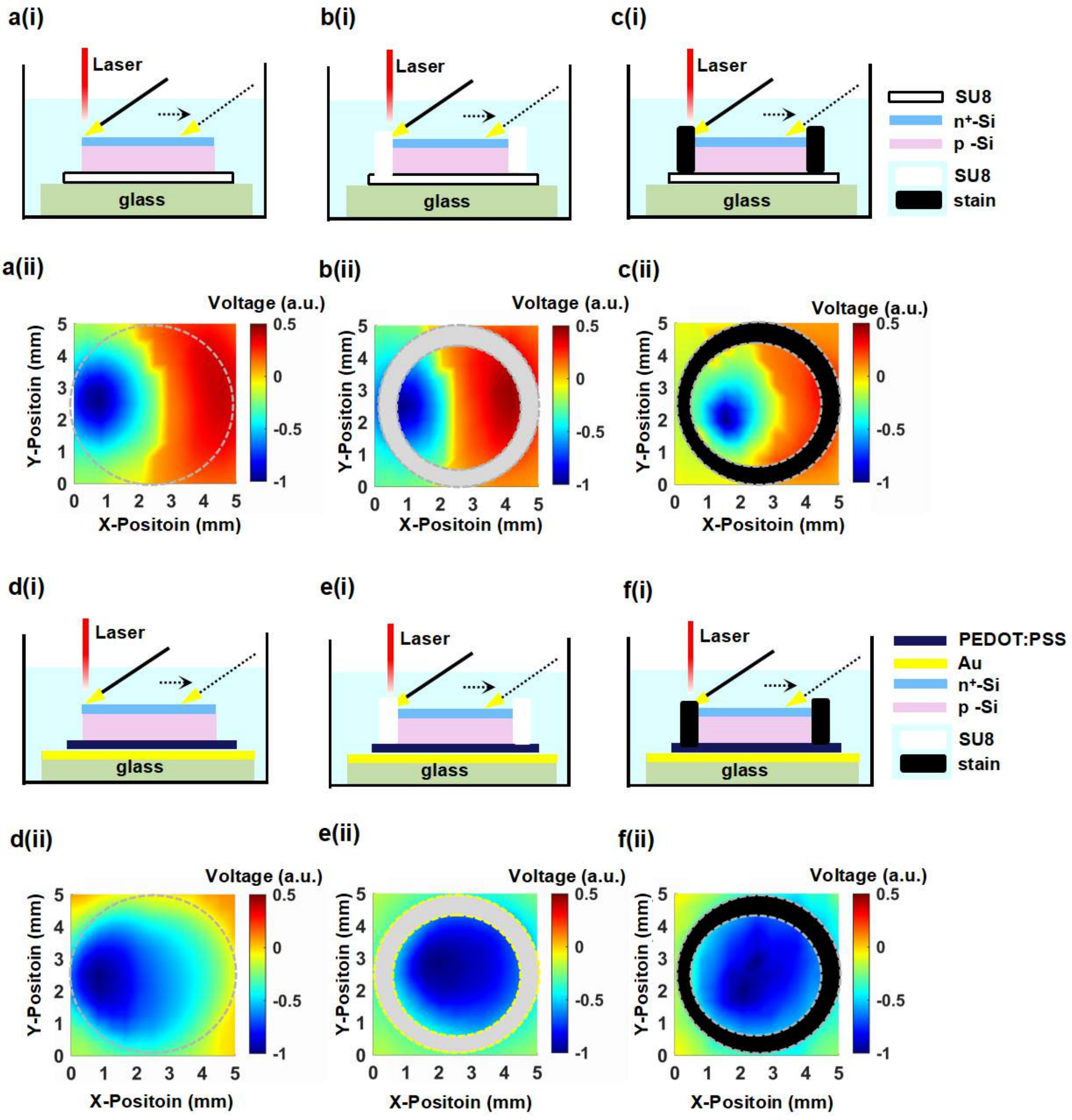

**Figure S4. Boundary effects on surface voltage distribution in illuminated silicon membranes.** All measurements: 5 mm diameter pn$^+$ silicon (25 µm thick, $1\times10^{15}$ ions/cm$^2$ dose) under 10 mW left-edge illumination. a) b) c) Glass/SU8 substrates: a) Uncoated: i) schematic and ii) voltage heatmap. b) SU8-coated: i) schematic and ii) voltage heatmap. c) Light-blocking coated: i) schematic and ii) voltage heatmap. d) e) f) Au/PEDOT:PSS substrates: d) Uncoated: i) schematic and ii) voltage heatmap. e) SU8-coated: i) schematic and ii) voltage heatmap. f) Light-blocking coated: i) schematic and ii) voltage heatmap.

# Figure S5

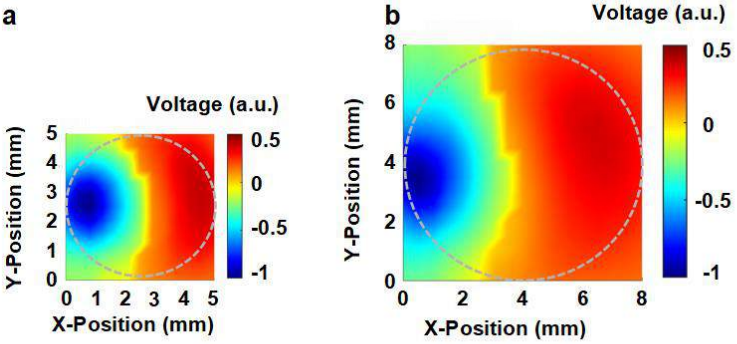

**Figure S5. Size-dependent voltage distribution in silicon membranes.** a) Voltage heatmap for 5 mm diameter membrane. b) Voltage heatmap for 8 mm diameter membrane.

# Figure S6

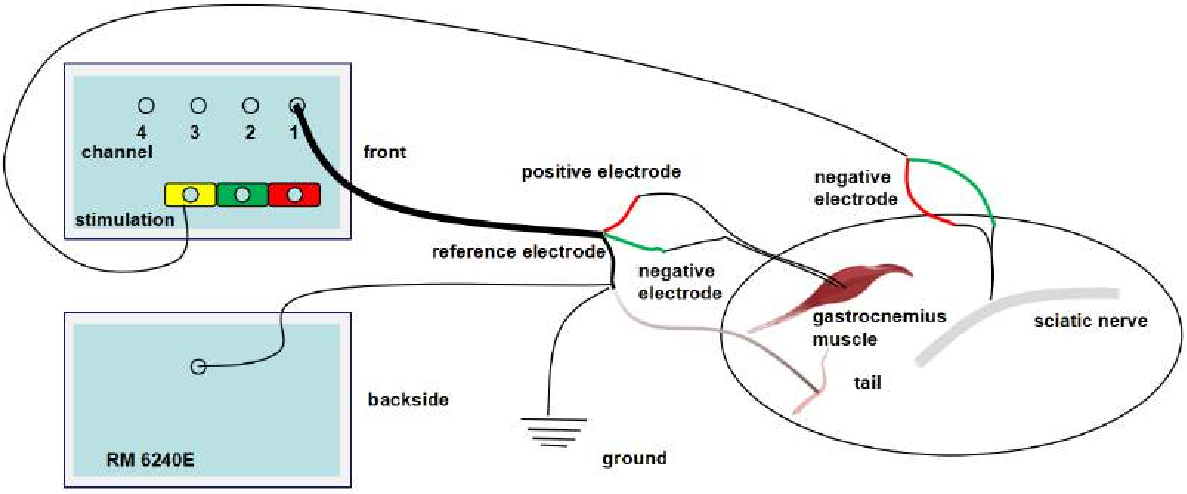

**Figure S6. Schematic of the experimental connection configuration for EMG measurements.**

# Figure S7

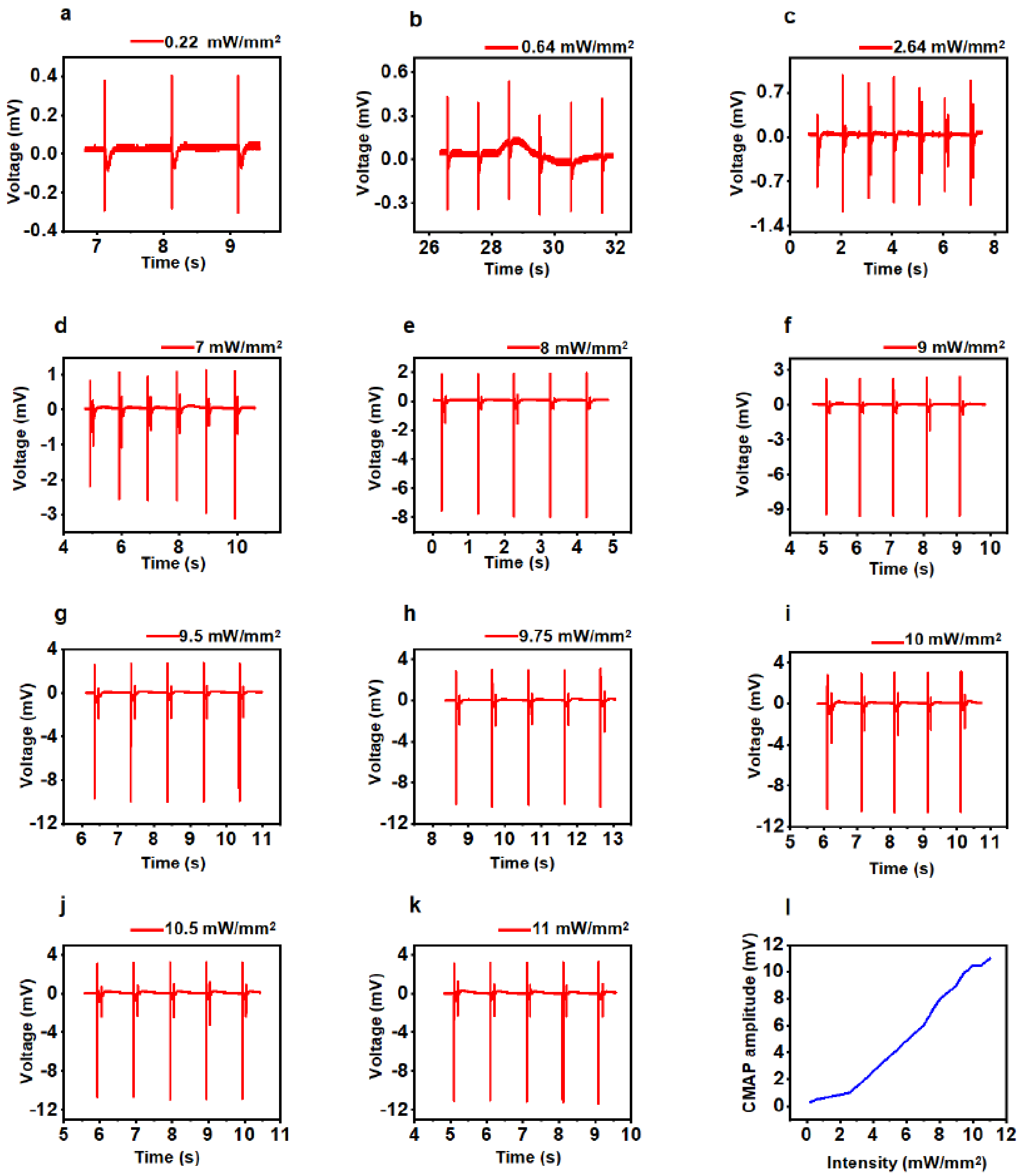

**Figure S7. Intensity-dependent CMAP responses to optoelectronic stimulation.** a) 0.22 mW/mm$^2$. b) 0.64 mW/mm$^2$. c) 2.64 mW/mm$^2$. d) 7 mW/mm$^2$. e) 8 mW/mm$^2$. f) 9 mW/mm$^2$. g) 9.5 mW/mm$^2$. h) 9.75 mW/mm$^2$. i) 10 mW/mm$^2$. j) 10.5 mW/mm$^2$. k) 11 mW/mm$^2$. l) CMAP amplitude shows an intensity-dependent increase.

# Movies S1

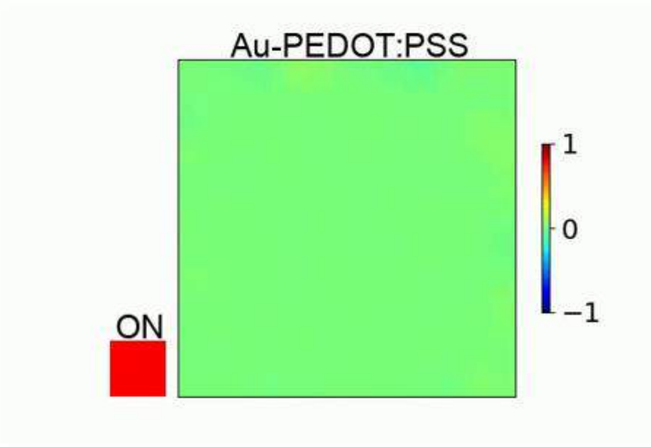

**Movies S1. Dynamic surface voltage redistribution in conductive substrate silicon films.** Time-resolved 2D heatmap showing voltage changes during laser activation and deactivation (Au/PEDOT: PSS substrate).

# Movies S2

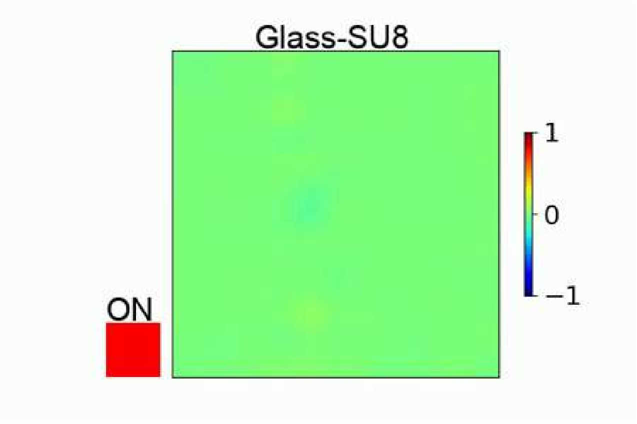

**Movies S2. Dynamic surface voltage redistribution in non-conductive substrate silicon films.** Time-resolved 2D heatmap showing voltage changes during laser activation and deactivation (Glass/SU8 substrate).

# Movies S3

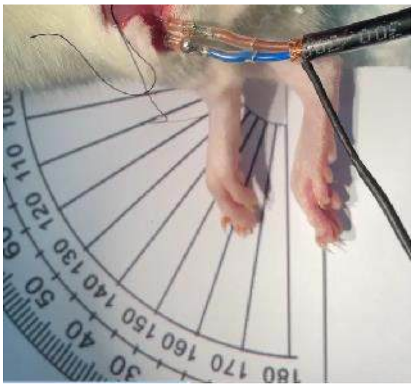

**Movies S3. High-speed kinematic analysis of optoelectronic stimulation efficiency.** Limb displacement quantification using high-speed imaging to assess stimulus response dynamics.

# Movies S4

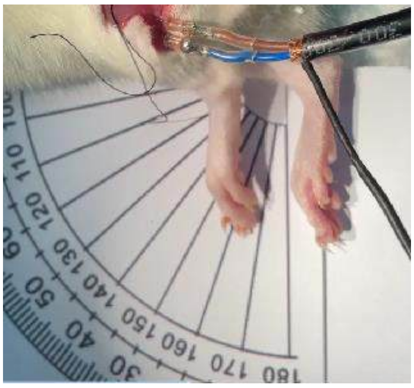

**Movies S4. Slow-motion video (0.1 × speed) demonstrates the limb movement.**